No. 662 **April 2023**

Numerical study of the RBF-FD method for the Stokes equations

A. Westermann, O. Davydov,
A. Sokolov, S. Turek

ISSN: 2190-1767

Numerical study of the RBF-FD method for the Stokes equations

Alexander Westermann* Oleg Davydov*

Andriy Sokolov** Stefan Turek**

April 24, 2023

Abstract

We study the numerical behavior of the meshless Radial Basis Function Finite Difference method applied to the stationary incompressible Stokes equations in two spatial dimensions, using polyharmonic splines as radial basis functions with a polynomial extension on two separate node sets to discretize the velocity and the pressure. On the one hand, we show that the convergence rates of the method correspond to the known convergence rates of numerical differentiation by the polyharmonic splines. On the other hand, we show that the main condition for the stability of the numerical solution is that the distributions of the pressure nodes has to be coarser than that of the velocity everywhere in the domain. There seems to be no need for any complex assumptions similar to the Ladyzhenskaya-Babuška-Brezzi condition in the finite element method. Numerical results for the benchmark driven cavity problem are in a good agreement with those in the literature.

Key words: meshless methods, polyharmonic splines, RBF-FD, Stokes equations, driven cavity problem

*Department of Mathematics, JLU Giessen, Email addresses: alexander.westermann@math.uni-giessen.de, oleg.davydov@math.uni-giessen.de.

**Institute for Applied Mathematics, TU Dortmund, Email addresses: andriy.sokolov@math.tu-dortmund.de, ture@featflow.de.

1 Introduction

Standard methods for approximating the numerical solution of partial differential equations are mesh-dependent and their performance is strongly influenced by the quality of the mesh. This becomes a considerable drawback when either a lot of work concerning reconstruction, refinement or alignment of the mesh during the simulation phase is necessary, or when there is not enough information or time to construct an appropriate mesh during the preprocessing phase. To overcome this restriction, a variety of meshless methods have been proposed, see, e.g., the review articles [3, 12, 18, 21].

One of the most promising meshless approaches is the radial basis function finite difference (RBF-FD) method suggested by Tolstykh and Shirobokov in 2003 [29]. Rapidly growing research on this method demonstrates that the RBF-FD method is capable to deliver accurate numerical solutions for complex problems, e.g., geo-modeling on spheres such as the simulation of the shallow-water equations [16, 17], the incompressible Navier-Stokes equations [15], or the reaction-diffusion-convection equations on manifolds [26, 27].

One of the issues that has not been sufficiently addressed in the RBF-FD community remains in the application to saddle point problems and its stability. In this paper, we focus on the Stokes equations and its velocity and pressure solution as one of the most important representatives of this class. In the finite element method, the answer to the stability question is obtained with the help of the well-known Ladyzhenskaya-Babuška-Brezzi (LBB) condition, see e.g. [5]. Recall that LBB describes a complicated interplay between finite element spaces used for discretizing velocity and pressure. Only those pairs of finite element spaces for which LBB is known to hold are recommended for the practical use in solving the Stokes equations. A major goal of our work was to identify stability conditions in numerical experiments that can serve as an analogue of LBB for the RBF-FD methods. Our experiments suggest that the only condition to be met is that the discretization nodes for the velocity should be denser than those for the pressure everywhere in the computational domain. In particular, the degrees of the polynomial extensions are only relevant for the convergence order, but have no influence on the stability.

The second point of interest in this paper is the accuracy of the resulting method and whether convergence orders expected from the theory and numerical experiments of numerical differentiation by RBFs are confirmed for the saddle point system of the Stokes equations.

The paper is organized as follows. In Section 2, we briefly describe the RBF-FD method based on polyharmonic splines (PHS) with polynomial extension. After that, in Section 3 we discuss discretization aspects for the Stokes equations, in particular how to handle non-uniqueness of the pressure

numerically. The numerical experiments are divided into two parts. In the first part (Section 4), we run a number of experiments for a test problem with a known smooth solution in order to investigate stability and convergence properties of the RBF-FD method for various choices of the discretization parameters for velocity and pressure. In the second part, see Section 5, we demonstrate the performance of the method for a well-known benchmark problem, the driven cavity problem (DCP). The last Section 6 is dedicated to a short conclusion.

2 Radial Basis Function Finite Difference Method

Meshless kernel-based finite difference discretizations of a linear differential operator $\mathcal{D}$ acting on scalar valued functions u in a computational domain $\Omega \subset \mathbb{R}^d$ are obtained in the following way. The derivation with respect to a vector valued function $\boldsymbol{u}$ is done similarly.

In the first step, we choose a set of N nodes in $\overline{\Omega}$

$$\Omega_N := \{\boldsymbol{z}_i : i = 1, \ldots, N\} \subset \overline{\Omega}.$$

For a recent survey on how to generate suitable discretizations Ω_N of a computational domain Ω, see [28].

In the second step, $\mathcal{D}u(\boldsymbol{z}_i)$ is approximated as a linear combination of the values $u(\boldsymbol{z}_k)$ at $\boldsymbol{z}_k \in \Omega_N$ with coefficients (*weights*) $\omega_{i,k}$,

$$\mathcal{D}u(\boldsymbol{z}_i) \approx \mathcal{D}_N u(\boldsymbol{z}_i) := \sum_{k=1}^{N} \omega_{i,k} u(\boldsymbol{z}_k). \tag{1}$$

In contrast to the classical FDM, the numerical differentiation weights $\omega_{i,k}$ are not predefined by a stencil, but are instead found by solving a certain linear system for each $\boldsymbol{z}_i$. More precisely, for each $\boldsymbol{z}_i$ we choose a *set of influence* $S_i \subset \{1, \ldots, N\}$ with $\#S_i \ll N$ and assume that

$$\omega_{i,k} = 0 \text{ for all } k \notin S_i.$$

The weights $\omega_{i,k}$ are obtained by requiring exactness of the numerical differentiation formula (1) for all functions of the form

$$u(\boldsymbol{x}) = \sum_{i=1}^{N} \alpha_i \Phi(\boldsymbol{x}, \boldsymbol{z}_i) + \sum_{k=1}^{M} \gamma_k p_k(\boldsymbol{x}) \tag{2}$$

satisfying

$$\sum_{i=1}^{N} \alpha_i p_k(\boldsymbol{z}_i) = 0, \quad k = 1, \dots, M \tag{3}$$

where α_i and γ_k are some coefficients, Φ is a conditionally positive definite kernel of order at most $m \in \mathbb{Z}_+$, and $\{p_k\}_{k=1}^M$ is a basis of the space $\Pi_m(\mathbb{R}^d)$ of d-variate polynomials of degree less than m, with dimension

$$M = \dim \Pi_m^d = \binom{m+d-1}{d}.$$

In the case $m = 0$ we get $M = 0$, which means that the polynomial extension in (2) and condition (3) disappears. Most kernels Φ used in this method are radial basis functions, in which case it is called *radial basis function finite difference method* [17].

Recall that a symmetric kernel $\Phi : \mathbb{R}^d \times \mathbb{R}^d \to \mathbb{R}$ is said to be *conditionally positive definite* of order s if for any finite set $\{\boldsymbol{x}_1, \dots, \boldsymbol{x}_n\} \subset \mathbb{R}^d$ the quadratic form $\sum_{i,j=1}^n \alpha_i \alpha_j \Phi(\boldsymbol{x}_i, \boldsymbol{x}_j)$ is positive for all $\boldsymbol{\alpha}$ such that $\sum_{i=1}^n \alpha_i p(\boldsymbol{x}_i) = 0$ for all $p \in \Pi_s(\mathbb{R}^d)$. In the case $s = 0$ we have $\Pi_0(\mathbb{R}^d) = \{0\}$ and the kernel Φ is said to be (unconditionally) *positive definite*. A positive definite or conditionally positive definite kernel Φ is called a *radial basis function* if $\Phi(\boldsymbol{x}, \boldsymbol{y}) = \phi(\|\boldsymbol{x} - \boldsymbol{y}\|)$, $\boldsymbol{x}, \boldsymbol{y} \in \mathbb{R}^d$, for some function $\phi : \mathbb{R}_+ \to \mathbb{R}$. The use of RBFs is an established tool for the interpolation of multivariate data at scattered points, see [6, 14, 30].

The exactness of (1) for all functions u of the form (2) satisfying (3) is equivalent (see [8]) to the following linear system with respect to the unknown weights $\omega_{i,k}$ and polynomial coefficients γ_k,

$$\sum_{k \in S_i} \omega_{i,k} \Phi(\boldsymbol{z}_j, \boldsymbol{z}_k) + \sum_{k=1}^{M} \gamma_k p_k(\boldsymbol{z}_j) = \mathcal{D}_1 \Phi(\boldsymbol{z}_i, \boldsymbol{z}_j), \quad j = 1, \dots, N \tag{4}$$

$$\sum_{k \in S_i} \omega_{i,k} p_j(\boldsymbol{z}_k) = \mathcal{D} p_j(\boldsymbol{z}_i), \quad j = 1, \dots, M, \tag{5}$$

where $\mathcal{D}_1$ means that $\mathcal{D}$ is applied to the first argument of the kernel Φ. According to [8] there exists a unique vector of weights $[\omega_{i,k}]_{k=1}^N$ satisfying (4) and (5) as soon as there is any solution to the linear system (5). This condition is often significantly weaker than the standard approach [30] of requiring the unisolvence of the set $\{\boldsymbol{z}_k\}_{\in S_i}$ with respect to the polynomial space $\Pi_m(\mathbb{R}^d)$. In particular, it provides RBF-FD weights for the Laplacian $\mathcal{D} = \Delta$ on certain 'deficient' sets with cardinality less than M, making the method less sensitive to the choice of the sets of influence S_i.

Although positive definite RBFs, e.g. the Gaussian function $\phi(r) = e^{-(\epsilon r)^2}$, have the advantage that no polynomial term is needed and there is no restriction on the sets of influence, they are very sensitive to the choice of the shape parameter ϵ and suffer from high condition numbers for the computation of the weights $\omega_{i,k}$ when the distances between nodes in the set of influence become small. Therefore, we use PHS $\phi(r) = r^\ell$ with an odd $\ell \in \mathbb{N}$, which are conditionally positive definite of order $\lfloor \ell/2 \rfloor + 1$, see [2] for a comprehensive discussion of their advantages in the RBF-FD method.

The right choice of the set of influence S_i is important for an efficient performance of the method. It includes both the cardinality of S_i and a reasonable selection of its nodes, e.g. to avoid one-sided constellations, especially if Ω_N is rather irregular. On the one hand, the set of influence should not be too small to ensure solvability of (5) and reasonable accuracy of the numerical differentiation formula (1). On the other hand, it should not be too large to keep the computation time low. Elaborate algorithms for the selection of the sets of influence to be as small as possible without compromising the accuracy, have been proposed, e.g., in [7, 9, 10, 22], and allow in particular a competitive performance of RBF-FD with respect to the sparsity of the system matrices for the Poisson problem. For the sake of simplicity in this paper we follow the suggestion of [2] that choosing $\{\boldsymbol{z}_k\}_{k \in S_i}$ as the set of at least $2M$ nearest neighbors of $\boldsymbol{z}_i$ produces a good influence set if the nodes in Ω_N are well distributed.

In the third step, the computed weights are used in a global system to find the approximations of the unknown values $u(\boldsymbol{z}_i)$, which is similar to the classical FD approach.

3 Discretization of the Stokes problem

We consider the bivariate stationary incompressible Stokes equations in the primitive variable form. The corresponding system of differential equations reads:

$$-\Delta \boldsymbol{u} + \nabla p = \boldsymbol{f} \tag{6}$$

$$\nabla \cdot \boldsymbol{u} = 0 \tag{7}$$

where $\boldsymbol{u}$ is the velocity vector field in two dimensions, p is the scalar pressure p and $\boldsymbol{f}$ is an external force.

In this work we treat the discretization of the velocity and pressure differently, so that we have two discretized domains: $\Omega_{\boldsymbol{u}}$ with the number of degrees of freedom $N_{\boldsymbol{u}} = \#\Omega_{\boldsymbol{u}}$ and Ω_p with $N_p = \#\Omega_p$. Similar to the notation of the previous section, we identify $S_{i,\Delta}$ and $S_{i,\nabla\cdot}$ as the sets of influence for the

Laplacian and divergence operators, respectively, corresponding to the node $\boldsymbol{z}_i \in \Omega_{\boldsymbol{u}}$, and $S_{i,\nabla}$ as the set of influence for the gradient operator corresponding to the node $\boldsymbol{z}_i \in \Omega_p$. All operators can be treated componentwise, and so the weights in (1) are computed for each component using the RBF-FD method of Section 2.

By setting all weights of every operator together, we obtain the following strongly coupled system

$$\begin{pmatrix} \boldsymbol{L} & B \\ \boldsymbol{D} & 0 \end{pmatrix} \begin{pmatrix} \boldsymbol{u}_h \\ p_h \end{pmatrix} = \begin{pmatrix} \boldsymbol{f}_h \\ 0 \end{pmatrix} \tag{8}$$

to be solved for a velocity-pressure tuple $(\boldsymbol{u}_h, p_h)^T$. Here, $\boldsymbol{L} \in \mathbb{R}^{2N_{\boldsymbol{u}} \times 2N_{\boldsymbol{u}}}$ represents the discretized Laplace operator, $B \in \mathbb{R}^{2N_{\boldsymbol{u}} \times N_p}$ the gradient operator and $D \in \mathbb{R}^{N_p \times 2N_{\boldsymbol{u}}}$ the divergence operator. This system has the following two noticeable properties:

- Looking at the size of the matrix B we conclude that in the case $2N_{\boldsymbol{u}} < N_p$ the rank of the matrix of the system (8) is at most $4N_{\boldsymbol{u}}$, by $N_p - 2N_{\boldsymbol{u}}$ smaller than its size, which certainly makes the discretization unreasonable, see similar argumentation by Elman *et al.* [13, Chapter 3.3] in the case of the finite element method. Therefore, the relation $N_{\boldsymbol{u}} \geq N_p/2$ must always be respected. We will see in the numerical experiments that a stronger inequality $N_{\boldsymbol{u}} > N_p$ must be preserved in order not to lose the stability of the method.

- In contrast to the finite element method, the discretization of the Stokes equations with the RBF-FD method does not lead to a saddle point system in the classical sense, since $B \neq \boldsymbol{D}^T$, but to a generalized saddle point system as considered e.g. by Benzi *et al.* [4].

Because the Stokes and Navier-Stokes equations are commonly used to model a fluid in a special domain, for example in a tunnel [24], the velocity boundary conditions are often a mixture of Dirichlet (DC) and Neumann (NC) conditions. In the most cases we have an inflow (DC), an outflow (NC) and a so-called *no-slip boundary condition* where the velocity is set to zero (DC). A natural condition for the outflow boundary part is the *do-nothing boundary condition*

$$\partial_{\boldsymbol{n}} \boldsymbol{u} - p\boldsymbol{n} = 0.$$

This condition in particular makes the pressure unique. However, if this boundary condition is not used, then the pressure remains ambiguous up to a constant.

One application is the simulation of the Stokes equations in a closed domain where only Dirichlet boundary conditions are specified for the velocity so that its normal component is set to zero (so-called *enclosed flow*, see e.g. [13]). Then no in- or outflow region is defined, and the pressure is only unique up to a constant because it is not involved in any boundary condition. In particular, the *Driven Cavity Problem* (DCP) as a classic test case belongs to this class. In order to obtain a unique solution for the pressure, in this case we extend the system (8) with a *uniqueness condition*

$$x_{\boldsymbol{u}}^T \boldsymbol{u}_h + x_p^T p_h = x_f, \tag{9}$$

where $x_{\boldsymbol{u}} \in \mathbb{R}^{N_{\boldsymbol{u}}}$ and $x_p \in \mathbb{R}^{N_p}$ are appropriately chosen vectors, and x_f is a scalar. We need to exercise certain care when choosing this condition because it may generate some artifacts in the computed solution. There are different ways to realize the uniqueness condition which can be roughly divided into two categories. On the one hand, there are local conditions, e.g. setting only one (pressure) point to some nominal value. This may result in some local distortion of the solution shape, but there will be no artifacts away from this point. On the other hand, there are global conditions, e.g. a zero mean condition, which influence the solution globally so that no local artifacts can be seen in the entire solution.

By adding the new condition instead of the classical approach of overwriting rows in the system matrix, the new matrix is not quadratic anymore. Even though we can use least squares algorithms to solve such systems, and get very small residuals in our experiments, a quadratic system has a big advantage for large scale problems, since standard iterative solvers may be used. In order to get a quadratic structure of the matrix, we introduce a dummy variable $\gamma \in \mathbb{R}$, which we call the *uniqueness variable*, and two more vectors $y_{\boldsymbol{u}}$, y_p to fill a new linearly independent column of the matrix. We observe in the numerical experiments of Section 4 that γ is normally much smaller than the discretization error. The new system has the form

$$\begin{pmatrix} \boldsymbol{L} & B & y_{\boldsymbol{u}} \\ \boldsymbol{D} & 0 & y_p \\ x_{\boldsymbol{u}}^T & x_p^T & 0 \end{pmatrix} \begin{pmatrix} \boldsymbol{u}_h \\ p_h \\ \gamma \end{pmatrix} = \begin{pmatrix} \boldsymbol{f}_h \\ 0 \\ x_{\boldsymbol{f}} \end{pmatrix}. \tag{10}$$

An approach that worked well in most numerical tests was to use a zero mean for the pressure, e.g. $x_{\boldsymbol{u}} = y_{\boldsymbol{u}} = 0$, $x_{\boldsymbol{f}} = 0$ and $x_p = y_p = (1, \ldots, 1)^T \in \mathbb{R}^{N_p}$.

4 Numerical Test I - Stability & Convergence

In the first test, we analyze the stability and convergence of the RBF-FD method applied to the Stokes equations with a prescribed analytical solution. We investigate numerically how the number of nodes and their distribution in the computational domain influence the stability of the discrete problem. After that we study the convergence of the velocity and the pressure with respect to

- a fixed order of PHS and a varying order of polynomial extensions,
- a varying order of PHS and a fixed order of polynomial extensions.

The test problem for this section has the analytical solution

$$\boldsymbol{u}(x,y) = \begin{pmatrix} \sin(\pi x)\cos(\pi y) \\ -\cos(\pi x)\sin(\pi y) \end{pmatrix} \qquad \text{and} \qquad p(x,y) = \sin(\pi x)\cos(\pi y)$$

defined on the unit square $\Omega = [-1,1]^2$. It is easy to see that the velocity $\boldsymbol{u}$ satisfies the incompressibility condition (7). The external force in (6) associated with this solution is given by

$$\boldsymbol{f}(x,y) = \pi \begin{pmatrix} \pi\sin(\pi x)\cos(\pi y) + \cos^2(\pi x) \\ \pi\cos(\pi y)\sin(\pi x) - \sin^2(\pi y) \end{pmatrix}.$$

We set Dirichlet boundary conditions for the velocity on the whole boundary of the computational domain Ω. As a result, the pressure and the incompressibility are only discretized inside of Ω. The zero mean pressure condition is used for the uniqueness condition (9) and the attached column w.r.t. the uniqueness variable is chosen symmetrically.

4.1 Test: Stability Condition

First, we discretize the domain Ω by equidistantly placed nodes for both velocity and pressure variables:

$$\Omega_{\boldsymbol{u}} = \left\{ x_{ij} \in \Omega \,|\, x_{ij} = (-1 + ih_{\boldsymbol{u}}, -1 + jh_{\boldsymbol{u}})^T, \quad i,j = 0,\dots,\frac{2}{h_{\boldsymbol{u}}} \right\},$$
$$\Omega_p = \left\{ x_{ij} \in \Omega \,|\, x_{ij} = \left(-1 + \left(i+\frac{1}{2}\right)h_p, -1 + \left(j+\frac{1}{2}\right)h_p\right)^T, \quad i,j = 0,\dots,\frac{2}{h_p} - 1 \right\},$$

where $h_{\boldsymbol{u}}$ and h_p are the step sizes. The PHS

$$\Phi(x,y) = \|x-y\|_2^3$$

with a quadratic polynomial extension ($m_\kappa = 3$) is applied to all differential operators. The cardinality of the sets of influence is 20, which is greater than $2M = 12$, as suggested in Section 2.

In order to evaluate the stability of the solutions for different step sizes experimentally, the error in the maximum-norm is listed in Tables 1 and 2. In Table 3, the uniqueness variable γ is also provided and is equal to the value $\|y_p\|_\infty \cdot \gamma$.

$h_p \backslash h_{\boldsymbol{u}}$	2^{-1}	2^{-2}	2^{-3}	2^{-4}	2^{-5}	2^{-6}	2^{-7}	N_p
2^{-2}	7.006e-01	6.272e-02	1.597e-02	1.091e-02	7.973e-03	7.364e-03	7.261e-03	64
2^{-3}	7.344e-01	3.566e+00	1.384e-02	7.755e-03	3.969e-03	1.977e-03	9.893e-04	256
2^{-4}	6.348e-01	8.006e+00	1.422e+00	7.594e-03	3.946e-03	1.985e-03	9.915e-04	1024
2^{-5}	6.357e-01	8.028e+00	2.430e+00	3.128e+00	3.923e-03	1.983e-03	9.928e-04	4096
2^{-6}	6.419e-01	2.063e+00	9.628e-01	1.192e+00	1.745e+00	1.979e-03	9.927e-04	16384
2^{-7}	7.037e-01	1.687e+00	1.934e+00	1.876e+00	1.201e+00	3.349e+00	9.917e-04	65536
$N_{\boldsymbol{u}}$	25	81	289	1089	4225	16641	66049	

Table 1: Velocity error in the maximum norm.

$h_p \backslash h_{\boldsymbol{u}}$	2^{-1}	2^{-2}	2^{-3}	2^{-4}	2^{-5}	2^{-6}	2^{-7}	N_p
2^{-2}	Inf	3.219e+01	1.502e-01	8.917e-02	9.715e-02	9.284e-02	8.886e-02	64
2^{-3}	Inf	Inf	2.972e-01	1.092e-01	6.525e-02	3.926e-02	2.491e-02	256
2^{-4}	Inf	Inf	Inf	2.372e-01	6.211e-02	3.336e-02	1.876e-02	1024
2^{-5}	Inf	Inf	Inf	Inf	8.693e-02	3.202e-02	1.633e-02	4096
2^{-6}	Inf	Inf	Inf	Inf	Inf	3.852e-02	1.620e-02	16384
2^{-7}	Inf	Inf	Inf	Inf	Inf	Inf	2.768e-02	65536
$N_{\boldsymbol{u}}$	25	81	289	1089	4225	16641	66049	

Table 2: Pressure error in the maximum norm.

$h_p \backslash h_{\boldsymbol{u}}$	2^{-1}	2^{-2}	2^{-3}	2^{-4}	2^{-5}	2^{-6}	2^{-7}	N_p
2^{-2}	8.554e-02	-3.061e-03	-2.173e-04	1.651e-05	-2.597e-05	-1.543e-05	-1.048e-05	64
2^{-3}	-2.354e-02	-4.741e-01	-6.415e-04	-1.978e-05	2.037e-06	-3.883e-06	-2.503e-06	256
2^{-4}	-1.362e-02	-1.723e-03	-2.199e-03	-5.288e-05	-1.213e-06	8.337e-08	-1.578e-07	1024
2^{-5}	2.578e-02	1.209e-02	6.270e-04	-4.353e-04	-3.539e-06	-7.142e-08	2.183e-09	4096
2^{-6}	1.549e-02	4.339e-03	1.127e-03	1.407e-04	3.209e-05	-2.250e-07	-4.289e-09	16384
2^{-7}	1.168e-03	-6.043e-03	-5.080e-04	6.503e-04	-9.135e-06	6.317e-05	-1.414e-08	65536
$N_{\boldsymbol{u}}$	25	81	289	1089	4225	16641	66049	

Table 3: Uniqueness variable γ.

As expected, the values in both error tables demonstrate that in order to obtain a converging solution, the pressure has to be discretized coarser than

the velocity, so that $N_{\boldsymbol{u}} > N_p$ must be satisfied. This is consistent with the algebraic condition $N_{\boldsymbol{u}} \geq N_p/2$ mentioned in Section 3. It can also be observed that choosing $N_{\boldsymbol{u}} \gg N_p$ does not indicate a significant influence onto the stability. All in all, these numerical experiments show that the number of nodes for velocity and pressure must satisfy the following stability condition:

$$\frac{N_p}{N_{\boldsymbol{u}}} < 1, \tag{11}$$

where N_p has to be high enough to not undersample the domain.

A lower limit cannot be derived here, but our numerical experiments show that the above ansatz is stable at least for a relation of $\frac{64}{66049} \approx 10^{-3}$.

The values of the uniqueness variable γ are decreasing if N_p and/or $N_{\boldsymbol{u}}$ increase but they are not significantly high even in the unstable cases. This shows that γ is not a stability identifier but rather can be interpreted as an identifier for the overall discretization error.

Let us now focus on the local stability behavior. For example, in the case of the DCP, the flow of a fluid near corners or walls may have a complex vortex-like structure. In order to capture a high order behavior of velocity in such subdomains, one has to wisely distribute a significant quantity of velocity nodes there. At the same time, the number of pressure nodes has to remain bounded to guarantee the stability condition. To implement this, we attempt to reorganize the equidistant velocity nodes to get a finer node configuration near the boundary without changing $N_{\boldsymbol{u}}$ significantly as shown in Figure 1. As a result, the new velocity step size in the middle of the domain $h_{\boldsymbol{u}} = \frac{4}{51}$ is higher than the pressure one $h_p = \frac{1}{17}$. This has the effect that the solution of the pressure is mainly unstable, which in turn has a direct influence on the solution of the velocity as can be seen in Figure 2, even though the stability condition (11) is violated only locally. However, if the step size in the middle of the domain is adjusted so that (11) holds locally in every subdomain, see Figure 3, whereby the global degrees of freedom are not changed significantly, then the solution is stable, as can be seen in Figure 4 for the new velocity step size $h_{\boldsymbol{u}} = \frac{1}{18} < h_p$.

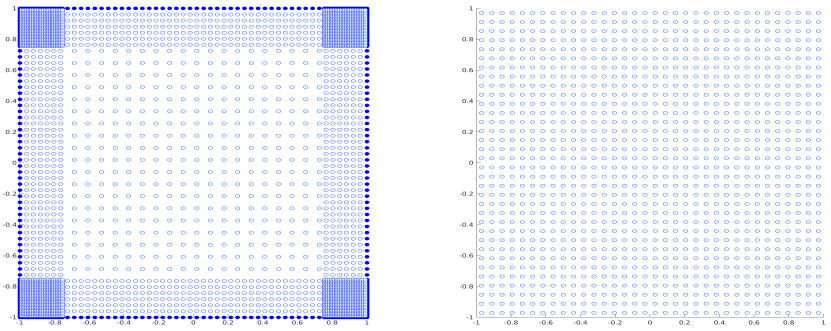

Figure 1: Structure of the locally refined node configuration for velocity (left) and pressure (right) with $N_{\boldsymbol{u}} = 4129$ and $N_p = 11567$.

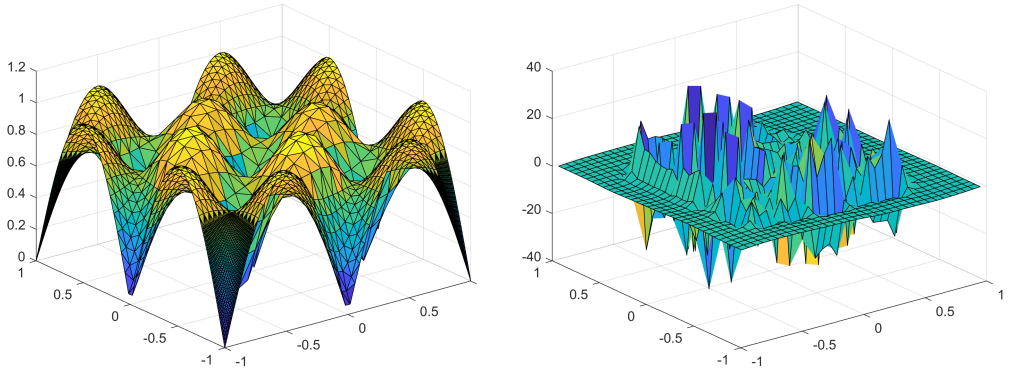

Figure 2: Solution for velocity (left) and pressure (right) for the locally refined nodes satisfying the stability condition (11) only globally with $N_{\boldsymbol{u}} = 4129$ and $N_p = 1156$.

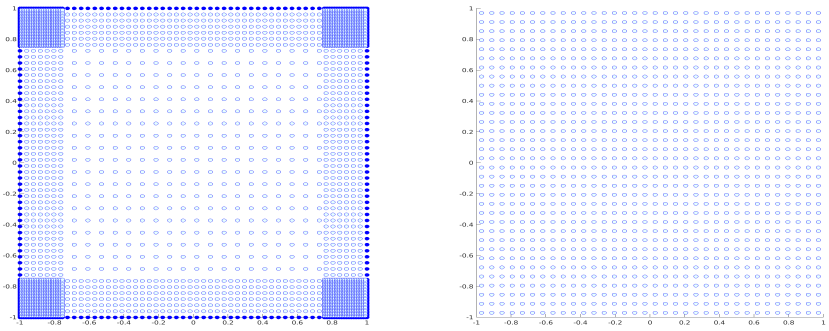

Figure 3: Structure of the locally refined node configuration for velocity (left) and pressure (right) with $N_{\boldsymbol{u}} = 4145$ and $N_p = 1156$.

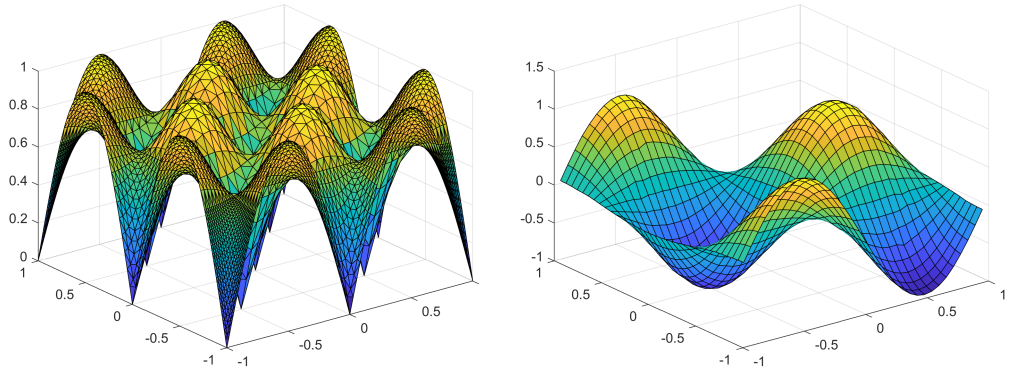

Figure 4: Node configuration for velocity (left) and pressure (right) for locally refined nodes satisfying the stability condition (11) locally, $N_{\boldsymbol{u}} = 4145$ and $N_p = 1156$.

4.2 Test: Convergence Analysis I

In this subsection, we study how the solution of the Stokes equations depends on the PHSs with fixed exponent and varying order of polynomial extensions. For discretization of velocity and pressure, equidistant steps with the relation $h_p = 2 \cdot h_{\boldsymbol{u}}$, resp. $N_p/N_{\boldsymbol{u}} = 0.25$, are chosen to satisfy (11). The experimental order of convergence is computed as

$$\mathrm{EoC} = \frac{\log\left(\frac{error_k}{error_{k+1}}\right)}{\log\left(\frac{h_k}{h_{k+1}}\right)} = \frac{\log\left(\frac{error_k}{error_{k+1}}\right)}{\log\left(2\right)}.$$

We use the fixed PHS

$$\Phi(x, y) = \|x - y\|_2^3$$

with the variable order of the polynomial extension $m_\kappa \in \{0, \ldots, 6\}$. Here, $m_\kappa = 0$ stands for no polynomial extension, $m_\kappa = 1$ stands for a polynomial extension with constant polynomials and so on. Because the accuracy of the RBF-FD method depends on the differential operator, we distinguish between $\kappa = 1$ for the first order operators (divergence of $\boldsymbol{u}$ and gradient of p) and $\kappa = 2$ for the second order of operator (Laplacian of $\boldsymbol{u}$). We adapt the size of the set of influence to m_κ according to Table 4, independently of whether velocity or pressure is discretized. In all cases the size is greater than $2M$.

m_κ	0	1	2	3	4	5	6
$\#S_{i,(\cdot)}$	10	10	10	20	25	35	50

Table 4: Cardinality of the set of influence of the operator $(\cdot)$ w.r.t. m_κ.

In Figures 5–11 we show the root mean square error (RMSE) of the velocity and the pressure. If one considers the plots corresponding to $m_1 = 0, \ldots, 6$, it is noticeable that the higher m_1, the better the convergence rate of the velocity and the pressure is for increasing m_2. At the same time, the velocity and the pressure do not converge for $m_1 < 2$ and $m_2 < 3$. This is consistent with the properties of the Stokes equations: The pressure only occurs in connection with the first order differentiation whereas the velocity with the first and the second order differentiation. If the order of the polynomial extension is less than the order of the differential operator, then the polynomial extension has no effect on the approximation and the pure application of the PHS is unstable.

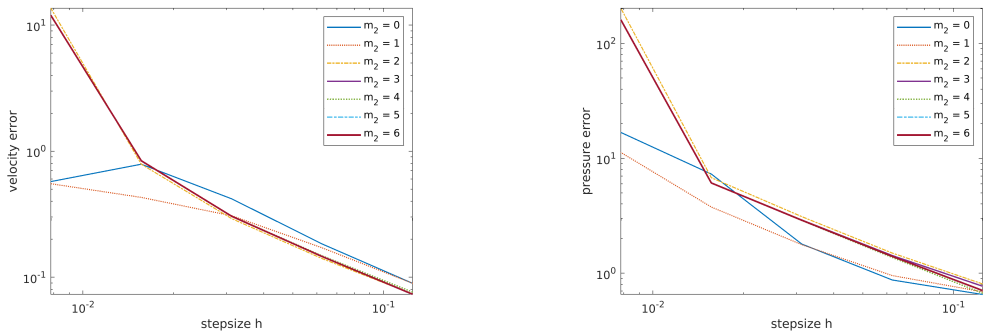

Figure 5: RMSE comparison for $m_1 = 0$ and various values of m_2 for velocity (left) and pressure (right).

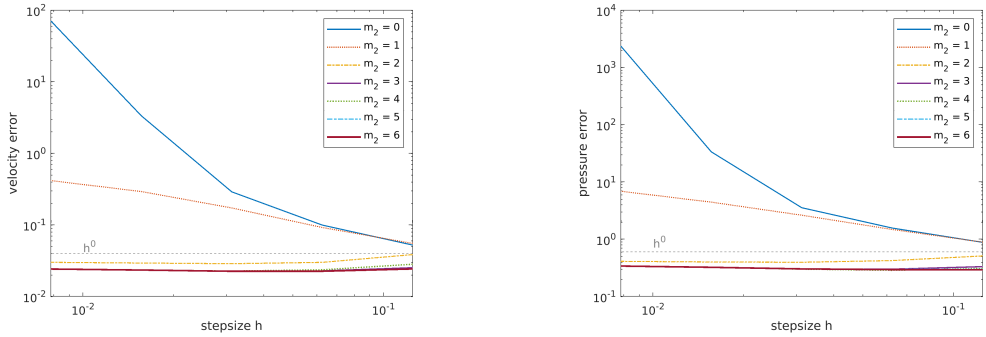

Figure 6: RMSE comparison for $m_1 = 1$ and various values of m_2 for velocity (left) and pressure (right).

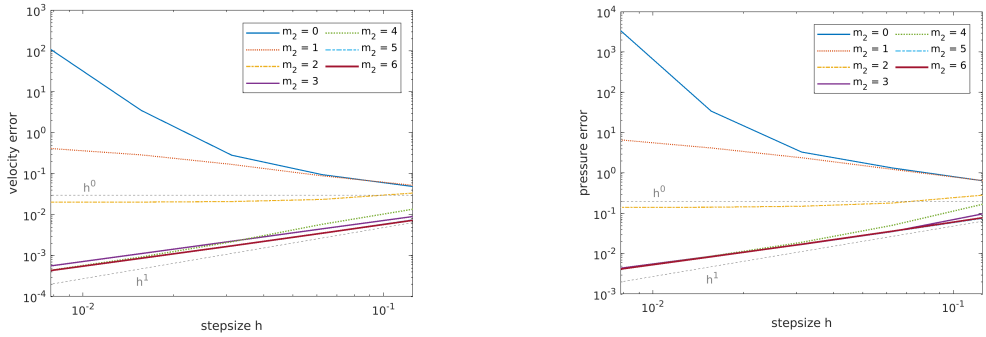

Figure 7: RMSE comparison for $m_1 = 2$ and various values of m_2 for velocity (left) and pressure (right).

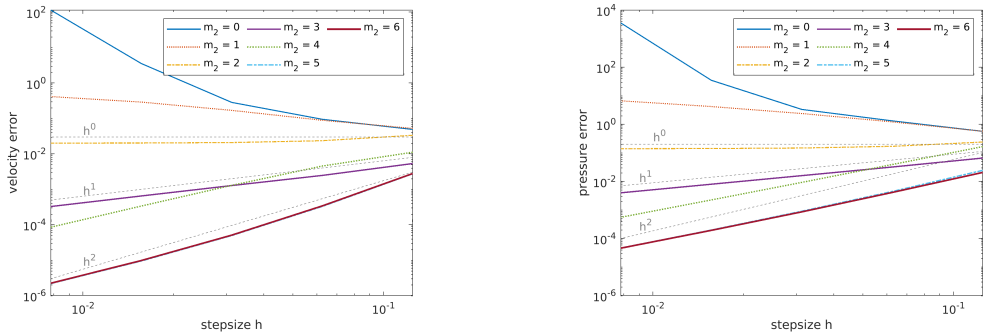

Figure 8: RMSE comparison for $m_1 = 3$ and various values of m_2 for velocity (left) and pressure (right).

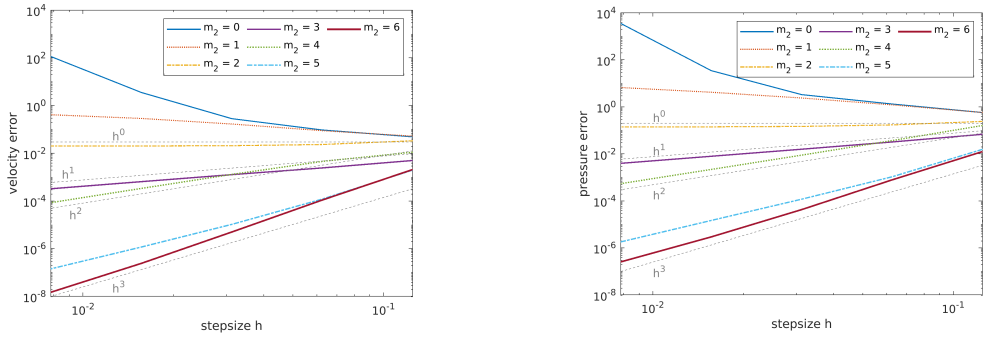

Figure 9: RMSE comparison for $m_1 = 4$ and various values of m_2 for velocity (left) and pressure (right).

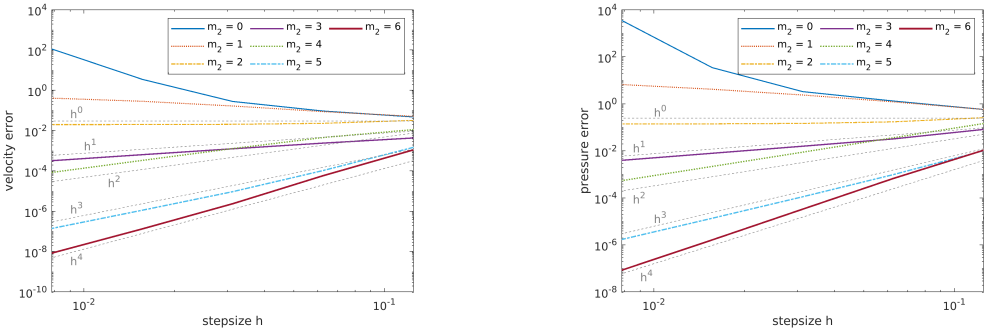

Figure 10: RMSE comparison for $m_1 = 5$ and various values of m_2 for velocity (left) and pressure (right).

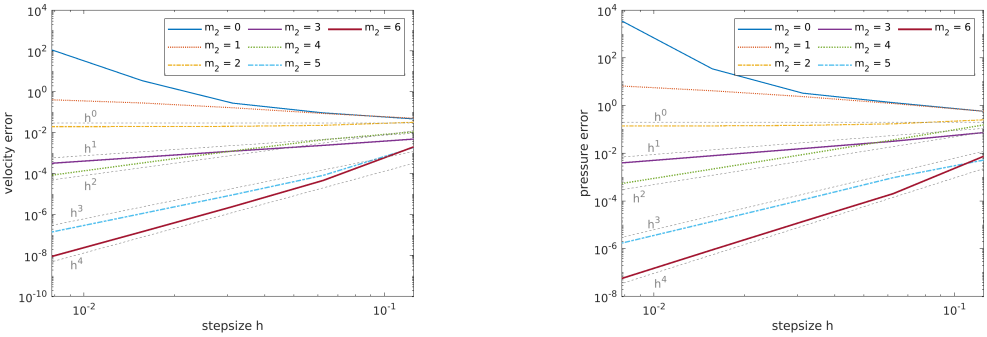

Figure 11: RMSE comparison for $m_1 = 6$ and various values of m_2 for velocity (left) and pressure (right).

To compare the convergence rates of the velocity and the pressure more precisely, the orders of convergence from the errors are listed in Table 5 where

each cell contains the order of convergence w.r.t. the velocity (left value) and the pressure (right value). The "n.s." stands for "not stable" and is consistent with the above reason for no convergence in the cases $m_1 = 0$ and $m_2 = 0, 1$. The special cases $m_1 = 1$ ($m_2 > 2$) and $m_2 = 2$ ($m_1 > 1$) get nonconverging solutions, too, but at the same time the approximation will not be worse when the step size reduces, so that we may speak of a "convergence rate of zero".

$m_2 \backslash m_1$	0	1	2	3	4	5	6
0	n.s.|n.s.	n.s.|n.s.	n.s.|n.s.	n.s.|n.s.	n.s.|n.s.	n.s.|n.s.	n.s.|n.s.
1	n.s.|n.s.	n.s.|n.s.	n.s.|n.s.	n.s.|n.s.	n.s.|n.s.	n.s.|n.s.	n.s.|n.s.
2	n.s.|n.s.	0|0	0|0	0|0	0|0	0|0	0|0
3	n.s.|n.s.	0|0	1|1	1|1	1|1	1|1	1|1
4	n.s.|n.s.	0|0	1|1	2|2	2|2	2|2	2|2
5	n.s.|n.s.	0|0	1|1	2|2	3|3	3|3	3|3
6	n.s.|n.s.	0|0	1|1	2|2	3|3	4|4	4|4

Table 5: Order of convergence for velocity (left value of each cell) and pressure (right value of each cell) with respect to m_1 and m_2.

From Figures 5–11 and Table 5 the following two concluding remarks can be drawn:

1. The convergence rates of the velocity and the pressure are approximately the same whereas the explicit error of the velocity is lower than that of the pressure. This might be explained by the fact that due to stability reasons we have to assign much fewer degrees of freedom to the pressure than to the velocity field.

2. The experimental order of convergence is

$$\mathrm{EoC} = \min\{m_1 - 1, m_2 - 2\}. \tag{12}$$

   Since smaller m_1, m_2 are preferable to achieve the same convergence order, the formula (12) suggests taking m_1 one lower than m_2, i.e. $m_2 = m_1 + 1$.

These numerical observations are consistent with those reported in the literature. In particular, in [17, Chapter 5.1.7], Fornberg and Flyer report the results of their numerical experiments showing that the numerical differentiation error for approximating the κ^{th} order derivatives by PHS and a polynomial extension up to order m_κ is of the size $O\left(h^{m_\kappa - \kappa}\right)$. Theoretical

results confirming the same rates are given in [11]. Therefore, the combined numerical differentiation error for velocity and pressure in $-\Delta \boldsymbol{u} + \nabla p$ is of the size $O(h^{m_1-1} + h^{m_2-2})$, which is in a good agreement with (12). Since we see the same rate for the numerical solution of the Stokes equation, this indicates a good stability of the method.

While analyzing the RMSE for the RBF-FD method, it is worth to take a look at the condition number of the global system matrix. Because of the non-symmetric property of the system matrix S, the condition number is computed with $\sqrt{cond_2(S^T S)}$. The corresponding results for different m_1 and $m_2 = m_1 + 1$ are shown in Table 6. It can be seen that the condition number increases by a factor of eight when the number of degrees of freedom is multiplied by four. It is remarkable that m_κ has no significant influence on the condition number although the cardinality of the set of influence and consequently the number of nonzero entries in the system matrix gets larger with increasing m_κ.

$m_1 \vert m_2$	1|2	2|3	3|4	4|5	5|6
$h_{\boldsymbol{u}} = 2^{-3}$	5.525e+04	4.627e+04	3.930e+04	4.405e+04	4.647e+04
$h_{\boldsymbol{u}} = 2^{-4}$	4.571e+05	3.802e+05	3.159e+05	3.586e+05	3.826e+05
$h_{\boldsymbol{u}} = 2^{-5}$	3.693e+06	3.065e+06	2.532e+06	2.884e+06	3.083e+06
$h_{\boldsymbol{u}} = 2^{-6}$	2.964e+07	2.459e+07	2.028e+07	2.311e+07	2.471e+07

Table 6: Condition numbers of the global system matrix, $m_1 = m_2 - 1$.

4.3 Test: Convergence Analysis II

In contrast to the previous chapter, we now focus on the question of how the solution of the Stokes equations depends on the PHSs with variable exponent and fixed order of polynomial extensions. We use the variable PHS

$$\Phi(x, y) = \|x - y\|_2^{\lambda_\kappa}$$

with the exponent $\lambda_\kappa \in \{3, 5, 7, 9\}$ and a polynomial extension of order 5. As in the previous chapter, the index κ indicates the order of a differential operator being discretized. Figures 12 and 13 show the RMSEs of velocity and pressure for $\lambda_1 \in \{3, 9\}$ and for different λ_2. The RMSEs for $\lambda_1 \in \{5, 7\}$ and different λ_2 have the same convergence behavior and are therefore not plotted separately. Note that the error of both, velocity and pressure, decreases if λ_2 increases. In the velocity case, the error of $\lambda_2 = 9$ is ten times lower than the error of $\lambda_2 = 3$. In general, the convergence rate does not increase if a

higher exponent is chosen. In contrast to λ_2, increasing λ_1 does not lead to any improvement of the velocity error, and only a slight improvement of the pressure error for larger step sizes.

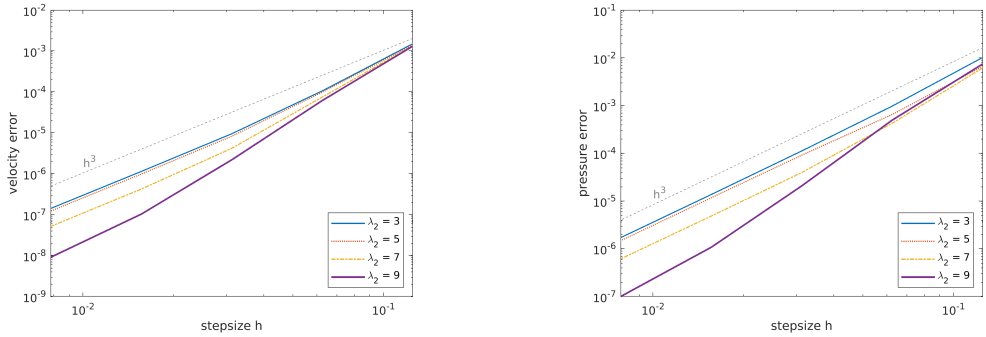

Figure 12: RMSE comparison for $\lambda_1 = 3$ and various values of λ_2 for velocity (left) and pressure (right).

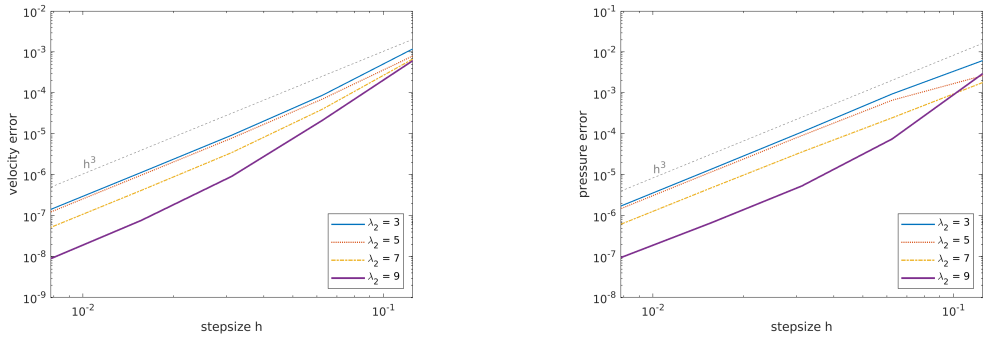

Figure 13: RMSE comparison for $\lambda_1 = 9$ and various values of λ_2 for velocity (left) and pressure (right).

After analyzing the convergence rates for various choices of λ_k, let us take a look at the behavior of the condition number of the global system matrix. The condition numbers for different choices of $\lambda_1 = \lambda_2$ are demonstrated in Table 7. It can be seen that the condition number does not depend significantly on the choice of the PHS exponent and behaves similarly to the test with increasing the polynomial order before.

$\lambda_1 \vert \lambda_2$	3|3	5|5	7|7	9|9
$h = 2^{-3}$	5.156e+04	4.527e+04	5.285e+04	6.707e+04
$h = 2^{-4}$	4.228e+05	3.724e+05	4.344e+05	5.503e+05
$h = 2^{-5}$	3.405e+06	3.005e+06	3.505e+06	4.439e+06
$h = 2^{-6}$	2.730e+07	2.411e+07	2.811e+07	3.560e+07

Table 7: Condition numbers of the global system matrix, $\lambda_1 = \lambda_2$.

4.4 Summary of Stability & Convergence Tests

Summarizing our results, on the one hand we see that the higher the order of the polynomial extension, the higher the convergence rate for velocity and pressure is. Furthermore, the polynomial extension for first order operators should be one lower than for second order operators, but it must be high enough so that the application of the differential operator does not annihilate the polynomial term. On the other hand, increasing the exponent does not increase the convergence order, but the exponent reduces the error at a numerical cost comparable to that of a lower exponent.

Thus, we may conclude that for the above smooth case a combination of a high exponent and a high polynomial order of the extension for all operators with $m_2 = m_1 + 1$ results in a convergent and stable combination to approximate the solution of the Stokes equations if the cardinality of the set of influence is adapted in a proper way and the relation (11) is not violated.

5 Numerical Test II - Driven Cavity

The smooth test case of the previous chapter does not represent a challenging problem. Therefore, in this chapter we consider a more complex representative of the Stokes equations - the Driven-Cavity-Problem (DCP). It arises, for example, in the modeling of a short-dwell coater [1] and generally describes the fluid motion in a restricted domain that is influenced only by a certain part of the boundary. For more details on the DCP, we refer to [19] by Kuhlmann and Romanò.

5.1 DCP on the unit square

In the first example we consider the unit square $\Omega = [-1, 1]^2$. The boundary $\Gamma = \partial\Omega$ is separated into two parts: the moving wall $\Gamma_m = [-1, 1] \times \{1\}$ and the solid wall $\Gamma_s = \Gamma \setminus \Gamma_m$. The velocity is subject to the following Dirichlet

boundary conditions:

$$\boldsymbol{u}(x,y)|_{\Gamma_s} = (0,0)^T \quad \text{and} \quad \boldsymbol{u}(x,y)|_{\Gamma_m} = (1,0)^T.$$

In order to get a unique solution for the pressure, one can exploit, e.g., the symmetry of the DCP for the Stokes equations by setting one point of the pressure at the centerline ($y = 0$) to zero. This symmetry is valid for the Stokes equations but not for the nonlinear Navier-Stokes equations. Therefore, we tend to the zero mean condition as in the previous tests, so that an extension to the Navier-Stokes equations is possible without any changes.

Following the quintessence of Chapter 4.4, we choose $\lambda_1 = \lambda_2 = 9$ and $m_1 = 5$, $m_2 = 6$. The sets of influence w.r.t. the differential operators are chosen from Table 4. From Figure 14, it can be seen that even with very few nodes the RBF-FD method delivers a reasonable approximation of the DCP, where the pressure is anti-symmetric at the vertical centerline and has singularities at the upper corners.

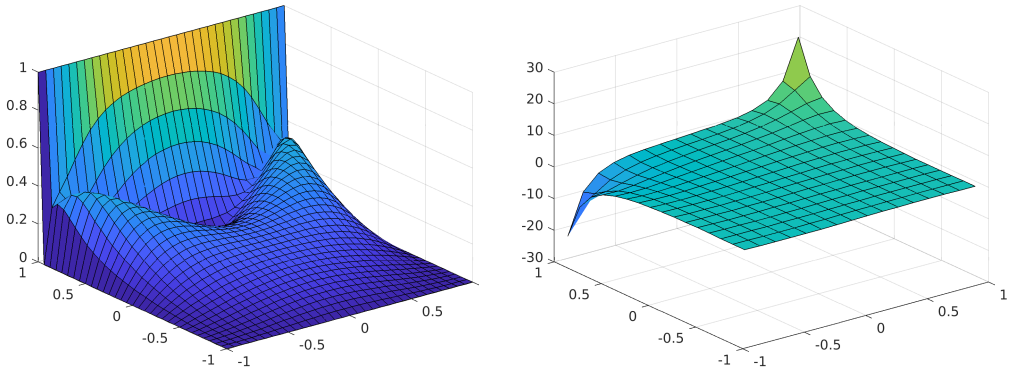

Figure 14: Solutions for the velocity (left) with $N_{\boldsymbol{u}} = 33^2$ and pressure (right) with $N_p = 16^2$.

Except of the zero vertical centerline of the pressure, there are no other exact values available to measure the numerical error. Nevertheless, it is possible to estimate the accuracy by adopting a very accurate solution obtained in Schumack *et al.* [25, Chapter 4] by a high order spectral method that takes into account a priori information about the strength of singularities of the pressure. The errors of our numerical solutions on equidistant discretizations for velocity and pressure against these reference solutions are presented in the third and fourth columns of Table 8. The errors are computed on the 11×11 equidistant grid tabulated in [25], excluding the pressure at the singularity corners. The last column of Table 8 contains the pressure RMSE at the

vertical centerline where the pressure vanishes. We see that all errors decrease monotonically whereby the global pressure error is higher in comparison to the other errors. This is in particular related to the coarser discretization of the pressure due to the stability condition. Another reason is its lower smoothness because of the singularities at the upper corners of the domain. Comparing to the results presented in the upper plots of Figure 9 of [25], we see that the velocity and pressure errors in Table 8 for our method are comparable to those in [25] for a comparable number of degrees of freedom when a spectral method without special treatment of corner singularities is applied even if the number of degrees of freedom for the pressure is much smaller than that used in [25].

$h_{\boldsymbol{u}}$	h_p	$RMS_{\boldsymbol{u}}$	RMS_p	$RMS_{p,centerline}$
2^{-3}	2^{-2}	1.382e-02	7.179e-01	2.361e-02
2^{-4}	2^{-3}	4.525e-03	4.932e-01	6.147e-03
2^{-5}	2^{-4}	2.669e-03	2.027e-01	1.708e-03
2^{-6}	2^{-5}	1.389e-03	2.681e-02	5.525e-04
2^{-7}	2^{-6}	6.970e-04	9.563e-03	2.461e-04

Table 8: RMSE of RBF-FD method vs. solution given in [25], and on the centerline.

Now, let us consider the properties of the velocity solution in the DCP. The motion of just one wall of the boundary has the effect that not only a big vortex appears in the middle of the domain, but also eddies of much smaller scale emerge at the bottom corners. These eddies are known as *Moffatt Eddies*, see e.g. [20]. In Figure 15, we demonstrate using the `streamslice` function of *MATLAB* how our RBF-FD method captures velocity streamlines in the case of an equidistant node configuration with $N_{\boldsymbol{u}} = 4225$ nodes for velocity and $N_p = 1024$ nodes for pressure which represents line 3 in Table 8. It should be mentioned that the streamlines looking like they were coming out of the boundary are artifacts of the visualization when the streamslice function is applied on a too coarse node configuration near the boundaries.

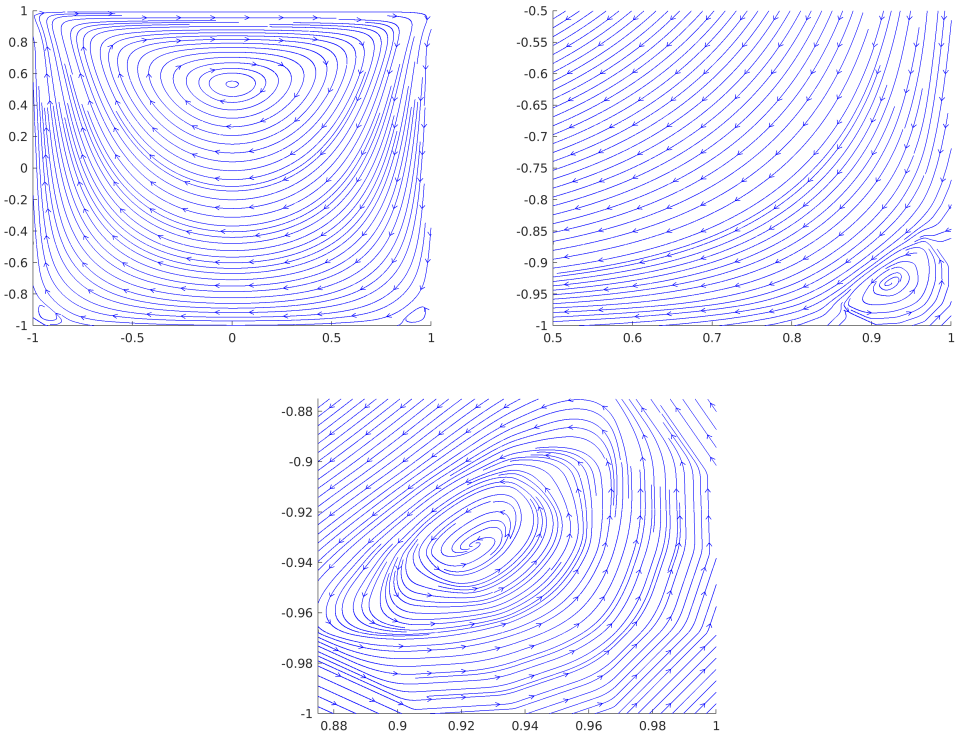

Figure 15: Streamlines of the velocity in the whole domain (upper-left), in the lower-right corner (upper right) and a zoomed version of the lower-right corner (below).

From the bottom plot of Figure 15, it can be seen that the Moffatt Eddy is not approximated accurately enough. This is due to the coarse velocity discretization near the corner of the computational domain. To get a better approximation, we exploit the meshless nature of the RBF-FD method by adding extra points in this subregion whereby the number of global degrees of freedom is approximately preserved and the relation (11) is not violated locally. An example of the new node configuration is visualized in Figure 16.

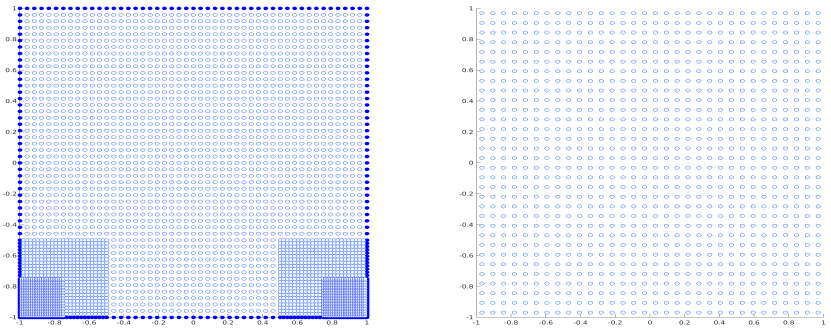

Figure 16: A corner-refined structure of nodes for velocity (left) and pressure (right).

In Figure 17, the velocity streamlines are visualized for the corner-refined case when $N_{\boldsymbol{u}} = 4225$ and $N_p = 1024$. One can see now that the Moffatt Eddies are significantly smoother and the second Moffatt Eddy can be guessed without getting any instabilities just by reordering the velocity nodes while respecting the stability condition.

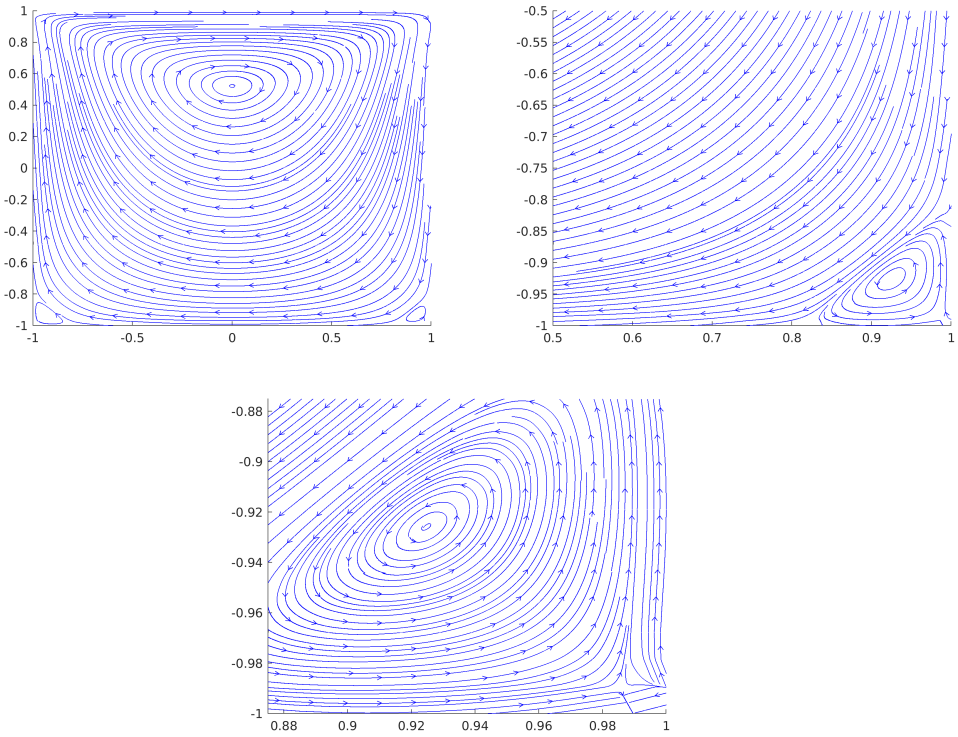

Figure 17: Streamlines of the velocity in the whole domain (upper-left), in the lower-right corner (upper-right) and zoomed version (below) for a corner-refined node configuration.

5.2 DCP on the wedge

Let us now use the RBF-FD method to approximate a fluid flow in a wedge between two lateral boundaries. The computational domain Ω belongs to a class of domains considered by Rønquist [23, Chapter 2.4.1]. It is a triangle with the vertices $(0, 2)$, $(1, 2)$ and $(0.5, 0)$. The boundary conditions are similar to those of the square domain with $\Gamma_m = [0, 1] \times \{2\}$ and $\Gamma_s = \Gamma \setminus \Gamma_m$. As in the square case, the pressure is singular at the upper corners and the velocity exhibits an infinite sequence of Moffatt Eddies.

We generate a sequence of discretizations obtained by repeated refinements of the initial velocity and pressure nodes shown in Figure 18. The velocity nodes are the vertices of quadrilaterals that are split into four subquadrilaterals in each refinement step, and the pressure nodes are the centroids of these quadrilaterals.

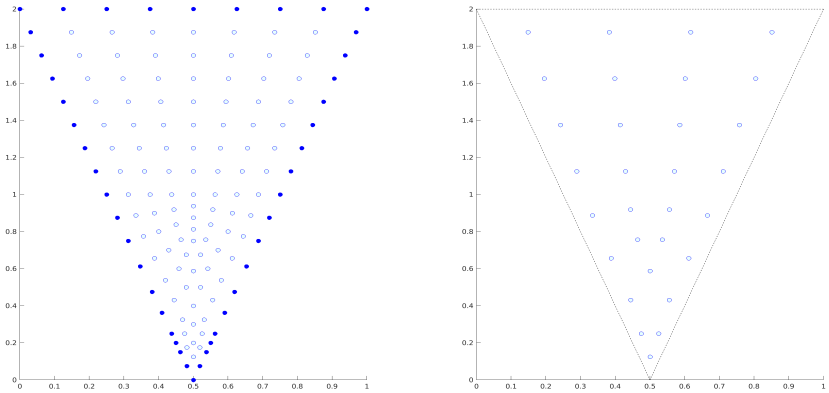

Figure 18: Initial node configuration for velocity (left) and pressure (right).

As in Chapter 5.1, we choose $\lambda_1 = \lambda_2 = 9$ and $m_1 = 5$ and $m_2 = 6$ with the related sizes of the sets of influence. In contrast to the above test with a square domain, we obtain the uniqueness condition (9) by setting the pressure at one node in the upper section near the centerline to zero. This has the advantage over a global zero mean condition that only one node or a local subarea is influenced by this artificial condition, so that the solution in the important areas, here the area near the wedge, is not distorted by this condition.

In Figure 19, the streamlines for the fifth refinement level are illustrated, where five Moffatt Eddies without a zoom and the sixth and the seventh eddies under the zoom can be observed.

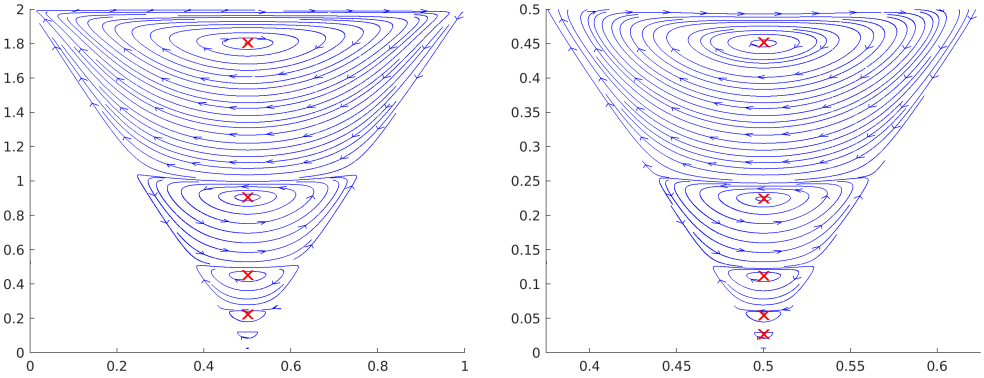

Figure 19: Streamlines of the velocity (left) and its zoomed version (right) for refinement level 5 with the local minima of the velocity of each Moffatt Eddy (red).

In [20, Chapter 3], Moffatt states that the eddies are in such a relation to each other that the distances r_n from the centers of the eddies to the wedge satisfy

$$\frac{r_n}{r_{n+1}} = \rho, \tag{13}$$

where $\rho > 0$ depends only on the angle of the wedge. Since the angle of the wedge is 28.07°, Moffatt's calculations result in $\rho \approx 2.01$. In Table 9 we present our estimates of r_n and ρ, where the center of each Moffat Eddy is computed as the corresponding local minimum of the velocity on the centerline. The minima are evaluated at interpolation points on the centerline with the step size 10^{-5}. Centers for the fifth level of the refinement are marked with red crosses in Figure 19. One can clearly observe that more Moffatt Eddies can be captured in the simulation with a larger number of nodes, and the approximations of ρ are in a good agreement with the results of Moffatt.

Moffatt Eddy	Level 1		Level 2		Level 3		Level 4		Level 5	
	r_n	ρ	r_n	ρ	r_n	ρ	r_n	ρ	r_n	ρ
1.	1.81250	-	1.81250	-	1.79688	-	1.80469	-	1.80469	-
2.	0.90625	2.00	0.90625	2.00	0.90625	1.98	0.90625	1.99	0.90625	1.99
3.	0.44844	2.02	0.44922	2.02	0.44922	2.02	0.44922	2.02	0.45220	2.00
4.	-	-	0.22500	2.00	0.22500	2.00	0.22500	2.00	0.22500	2.01
5.	-	-	0.11151	2.02	0.11211	2.01	0.11211	2.01	0.11211	2.01
6.	-	-	-	-	-	-	0.05654	1.98	0.05486	2.04
7.	-	-	-	-	-	-	-	-	0.02724	2.01

Table 9: Centers of the Moffatt Eddies and the related parameter ρ.

Similar to the case of the square domain, the symmetry of the pressure implies that it is zero on the vertical centerline, and this can serve as a good identifier for convergence. Corresponding values of the RMSEs for the pressure on the centerline for each level of refinement are shown in Table 10. We see that the error decreases significantly in each refinement.

Level	$RMSE_{p,\text{centerline}}$
1	7.490e-02
2	2.069e-02
3	5.606e-03
4	1.775e-03
5	8.498e-04

Table 10: RMSE of the pressure on the vertical centerline.

6 Conclusion

In this paper, the RBF-FD method with PHS radial basis functions has been applied to the incompressible stationary Stokes equations. We study various configurations of the polyharmonic splines and polynomial extensions. Through our numerical experiments, we make an attempt to experimentally derive a stability condition for the discretizations of the velocity and the pressure. The experiments show that the only stability condition is that the number of pressure points should be globally and locally smaller than the number of velocity points. Furthermore, if the order of the polynomial extension is chosen high enough so that the polynomial extension is not annihilated, there are no further stability conditions on the PHS. These results have shown that no stability conditions similar to the LBB condition are necessary, and may serve as a numerical background for future theoretical derivations, as well as guidelines for the generation of nodes with more complex configurations.

It is also shown that the convergence rate of the coupled velocity-pressure system depends only on the order of the polynomial extension, but not on the parameters of the polyharmonic splines. Nevertheless, the error can be further decreased by choosing a higher exponent of the PHS.

In comparison to the finite element method, the convergence rate can be increased simply by increasing the degree of the polynomial extension and increasing the size of the sets of influence, but without changing the discretization sets $\Omega_{\boldsymbol{u}}$ and Ω_p themselves. In particular, the nodes carry degrees of freedom of the solution, and do not need to be treated differently depending on whether they correspond to the interiors or edges or vertices of some geometric figures (elements), which complicates the implementation of the higher order finite element method.

As seen at the end of Section 5.2, the error also depends on the right choice of the set of influence. Here, further studies and experiments are required to investigate why and when a better approximation can be obtained by choosing the sets of influence in a more sophisticated way.

The application of the considered method to the driven cavity problems shows that it is capable of providing accurate numerical results for application-relevant benchmark test cases. Here, the meshless nature of the RBF-FD method in combination with the stability condition derived in preceding experiments makes it possible to obtain numerical results that compete well with those reported in the literature, and in particular reproduce a specific deep-vortex behavior established by analytical methods by *Moffatt* [20].

The use of an extra "uniqueness variable" to circumvent the uniqueness problem of the pressure in the case of the enclosed flow is a good alternative

to the classical approach by substituting a row of the system matrix. In particular, the resulting system matrix is non-singular.

All in all, we have demonstrated that the RBF-FD method with a high exponent of the PHS and a high order of the polynomial extension is a good candidate for simulating the Stokes equations. We expect that the settings of the RBF-FD method developed in this paper will be useful for the numerical solution of the nonlinear systems of the incompressible Navier-Stokes equations.

Acknowledgment

We would like to thank Dr. Christoph Lohmann from the TU Dortmund for valuable discussions regarding the Stokes equations and the treatment of the pressure uniqueness.

References

[1] C. K. Aidun, N. G. Triantafillopoulos, and J. D. Benson. Global stability of a lid-driven cavity with throughflow: Flow visualization studies. *Physics of Fluids*, 3(9):2081–2091, 1991. DOI https://doi.org/10.1063/1.857891.

[2] V. Bayona, N. Flyer, B. Fornberg, and G. A. Barnett. On the role of polynomials in RBF-FD approximations: II. Numerical solution of elliptic PDEs. *Journal of Computational Physics*, 332:257–273, 2017. DOI http://dx.doi.org/10.1016/j.jcp.2016.12.008.

[3] T. Belytschko, Y. Krongauz, D. Organ, M. Fleming, and P. Krysl. Meshless Methods: An Overview and Recent Developments. *Computer Methods in Applied Mechanics and Engineering*, 139(1-4):3–47, 1996. DOI http://dx.doi.org/10.1016/S0045-7825(96)01078-X.

[4] M. Benzi, G. H. Golub, and J. Liesen. Numerical solution of saddle point problems. *Acta Numerica*, 14:1–137, 2005. DOI http://dx.doi.org/10.1017/S0962492904000212.

[5] D. Braess. *Finite Elemente: Theorie, schnelle Löser und Anwendungen in der Elastizitätstheorie*. Springer-Verlag, 2013. DOI http://dx.doi.org/10.1007/978-3-642-34797-9.

[6] M. D. Buhmann. *Radial Basis Functions: Theory and Implementations*, volume 12. Cambridge University Press, 2003. DOI http://dx.doi.org/10.1017/CBO9780511543241.

[7] O. Davydov. Selection of Sparse Sets of Influence for Meshless Finite Difference Methods. *arXiv preprint arXiv:1908.01567*, 2019. URL https://arxiv.org/abs/1908.01567.

[8] O. Davydov. Approximation with Conditionally Positive Definite Kernels on Deficient Sets. In Marian Neamtu Gregory E. Fasshauer and Larry L. Schumaker, editors, *Approximation Theory XVI: Nashville 2019*, pages 27–38. Springer Berlin Heidelberg, 2021. DOI http://dx.doi.org/10.1007/978-3-030-57464-2_3.

[9] O. Davydov, D. T. Oanh, and N. M. Tuong. Improved Stencil Selection for Meshless Finite Difference Methods in 3D. *Journal of Computational and Applied Mathematics*, 425, 2023. DOI http://dx.doi.org/10.1016/j.cam.2022.115031.

[10] O. Davydov and M. Safarpoor. A meshless finite difference method for elliptic interface problems based on pivoted QR decomposition. *Applied Numerical Mathematics*, 161:489–509, 2021. DOI http://dx.doi.org/10.1016/j.apnum.2020.11.018.

[11] O. Davydov and R. Schaback. Optimal stencils in Sobolev spaces. *IMA Journal of Numerical Analysis*, 39(1):398–422, 2019. DOI https://doi.org/10.1093/imanum/drx076.

[12] C. A. Duarte. A Review of Some Meshless Methods to Solve Partial Differential Equations. Technical report, Texas Institute for Computational and Applied Mathematics Austin, TX, 1995. URL https://www.oden.utexas.edu/media/reports/1995/9506.pdf.

[13] H. C. Elman, D. J. Silvester, and A. J. Wathen. *Finite Elements and Fast Iterative Solvers: With Applications in Incompressible Fluid Dynamics*. Oxford University Press, 2014. DOI http://dx.doi.org/10.1093/acprof:oso/9780199678792.001.0001.

[14] G. E. Fasshauer. *Meshfree Approximation Methods with MATLAB*. World Scientific, 2007. DOI http://dx.doi.org/10.1142/6437.

[15] N. Flyer, G. A. Barnett, and L. J. Wicker. Enhancing finite differences with radial basis functions: Experiments on the Navier-Stokes equations.

J. Comput. Phys., 316:39–62, 2016. DOI https://doi.org/10.1016/j.jcp.2016.02.078.

[16] N. Flyer, E. Lehto, S. Blaise, G. B. Wright, and A. St-Cyr. A guide to RBF-generated finite differences for nonlinear transport: Shallow water simulations on a sphere. *Journal of Computational Physics*, 231(11):4078–4095, 2012. DOI http://dx.doi.org/10.1016/j.jcp.2012.01.028.

[17] B. Fornberg and N. Flyer. *A Primer on Radial Basis Functions with Applications to the Geosciences*. SIAM, 2015. DOI http://dx.doi.org/10.1137/1.9781611974041.

[18] T. Jacquemin, S. Tomar, K. Agathos, S. Mohseni-Mofidi, and S. Bordas. Taylor-series expansion based numerical methods: A primer, performance benchmarking and new approaches for problems with non-smooth solutions. *Archives of Computational Methods in Engineering*, 27:1465–1513, 2020. DOI https://doi.org/10.1007/s11831-019-09357-5.

[19] H. C. Kuhlmann and F. Romanò. The Lid-Driven Cavity. In A. Gelfgat, editor, *Computational Modelling of Bifurcations and Instabilities in Fluid Dynamics*, pages 233–309. Springer, Cham, 2019. DOI https://doi.org/10.1007/978-3-319-91494-7_8.

[20] H. K. Moffatt. Viscous and resistive eddies near a sharp corner. *Journal of Fluid Mechanics*, 18(1):1–18, 1964. DOI http://dx.doi.org/10.1017/S0022112064000015.

[21] V. P. Nguyen, T. Rabczuk, S. Bordas, and M. Duflot. Meshless methods: A review and computer implementation aspects. *Math. Comput. Simul.*, 79(3):763–813, 2008.

[22] D. T. Oanh, O. Davydov, and H. X. Phu. Adaptive RBF-FD Method for Elliptic Problems with Point Singularities in 2D. *Applied Mathematics and Computation*, 313:474–497, 2017. DOI http://dx.doi.org/10.1016/j.amc.2017.06.006.

[23] E. M. Rønquist. *Optimal spectral element methods for the unsteady three-dimensional incompressible Navier-Stokes equations*. PhD thesis, Massachusetts Institute of Technology, 1988. URL http://hdl.handle.net/1721.1/14365.

[24] M. Schäfer, S. Turek, F. Durst, E. Krause, and R. Rannacher. Benchmark Computations of Laminar Flow Around a Cylinder. In *Flow Simulation*

with High-Performance Computers II, pages 547–566. Springer, 1996. DOI http://dx.doi.org/10.1007/978-3-322-89849-4_39.

[25] M. R. Schumack, W. W. Schultz, and J. P. Boyd. Spectral Method Solution of the Stokes Equations on Nonstaggered Grids. *Journal of Computational Physics*, 94(1):30–58, 1991. DOI http://dx.doi.org/10.1016/0021-9991(91)90136-9.

[26] A. Sokolov, O. Davydov, D. Kuzmin, A. Westermann, and S. Turek. A flux-corrected RBF-FD method for convection dominated problems in domains and on manifolds. *Journal of Numerical Mathematics*, 27:253–269, 2019. DOI http://dx.doi.org/10.1515/jnma-2018-0097.

[27] A. Sokolov, O. Davydov, and S. Turek. Numerical study of the rbf-fd level set based method for partial differential equations on evolving-in-time surfaces. In M. Griebel and M. A. Schweitzer, editors, *Meshfree Methods for Partial Differential Equations IX*, pages 117–134. Springer International Publishing, Cham, 2019. DOI https://doi.org/10.1007/978-3-030-15119-5_7.

[28] P. Suchde, T. Jacquemin, and O. Davydov. Point Cloud Generation for Meshfree Methods: An Overview. *Archives of Computational Methods in Engineering*, 30:889–915, 2022. DOI https://doi.org/10.1007/s11831-022-09820-w.

[29] A. I. Tolstykh and D. A. Shirobokov. On using radial basis functions in a "finite difference mode" with applications to elasticity problems. *Computational Mechanics*, 33(1):68–79, 2003. DOI http://dx.doi.org/10.1007/s00466-003-0501-9.

[30] H. Wendland. *Scattered Data Approximation*. Cambridge University Press, 2004. DOI http://dx.doi.org/10.1017/CBO9780511617539.